

*This is a non-peer-reviewed preprint submitted to EarthArXiv.
The paper is undergoing peer-review for publication*

EarthArXiv Coversheet

Title: The Interplay of Vegetation and Land-Atmosphere Feedbacks in Flash Drought Prediction

Authors:

Mahmoud Osman^{*.1,2}; Benjamin Zaitchik³; Patricia Lawston-Parker^{2,4}; Joseph Santanello⁴; Martha
Anderson⁵

¹*Terrestrial Information Systems Laboratory, NASA Goddard Space Flight Center, Greenbelt, MD, USA*

²*Earth System Science Interdisciplinary Center, University of Maryland, College Park, MD, USA*

³*Department of Earth and Planetary Sciences, Johns Hopkins University, Baltimore, MD, USA*

⁴*Hydrological Sciences Laboratory, NASA Goddard Space Flight Center, Greenbelt, MD, USA*

⁵*Hydrology and Remote Sensing Laboratory, Agricultural Research Service, USDA, Beltsville, MD, USA*

Corresponding author; E-mail: mahosman01@gmail.com; Mahmoud.a.Osman@nasa.gov

This is a non-peer-reviewed preprint submitted to EarthArXiv.

The paper is undergoing peer-review for publication

The Interplay of Vegetation and Land-Atmosphere Feedbacks in Flash Drought Prediction

Mahmoud Osman^{1,2}; Benjamin Zaitchik³; Patricia Lawston-Parker^{2,4}; Joseph Santanello⁴; Martha Anderson⁵

¹*Terrestrial Information Systems Laboratory, NASA Goddard Space Flight Center, Greenbelt, MD, USA*

²*Earth System Science Interdisciplinary Center, University of Maryland, College Park, MD, USA*

³*Department of Earth and Planetary Sciences, Johns Hopkins University, Baltimore, MD, USA*

⁴*Hydrological Sciences Laboratory, NASA Goddard Space Flight Center, Greenbelt, MD, USA*

⁵*Hydrology and Remote Sensing Laboratory, Agricultural Research Service, USDA, Beltsville, MD, USA*

Abstract

Flash droughts, known for their rapid onset and intensification, pose a significant threat to agriculture and water resources. The 2011 Texas flash drought, with its widespread agricultural losses exceeding \$7.6 billion and severe ecological consequences, was a stark demonstration of their devastating impacts. This study investigates the crucial role of vegetation in numerical modeling of flash droughts, focusing on the 2011 Texas event. Utilizing the NASA Unified Weather Research and Forecasting (NU-WRF) and NASA Land Information System (LIS) modeling frameworks and the Noah Multi-Parameterization (Noah-MP) land surface model, we examine the influence of vegetation dynamics on simulating drought characteristics. By integrating satellite-derived vegetation observations and conducting controlled numerical experiments, we evaluate the model's ability to reproduce observed features of the 2011 drought. Our findings underscore the importance of vegetation representation in capturing the complex land-atmosphere feedbacks that drive the evolution of flash droughts. The incorporation of observed vegetation anomalies into the model leads to improved simulations of surface energy fluxes, atmospheric warming, and evapotranspiration patterns, particularly during the crucial onset and intensification phases of the drought. This points to the potential importance of representing vegetation variability in dynamically-based forecasts of flash drought.

29 **Introduction:**

30 Flash droughts, characterized by their rapid onset and intensification, pose a significant threat to
31 agriculture and water resources (Osman et al. 2021, 2022a; Otkin et al. 2018; Pendergrass et al.
32 2020; Svoboda et al. 2002). The swiftness of their development, often triggered by a
33 combination of precipitation deficits and anomalous atmospheric conditions such as heat waves
34 and high evaporative demand, makes them particularly difficult to predict and mitigate (Otkin et
35 al. 2013; Yuan et al. 2018; Zhang et al. 2017). The complex interplay between land surface
36 processes and atmospheric conditions during flash droughts underscores the potentially critical
37 role of vegetation in modulating these events (Jiang et al. 2024; Osman et al. 2022a,b).

38 Vegetation, through transpiration and its influence on surface energy fluxes, actively participates
39 in land-atmosphere feedback loops that can either amplify or dampen drought conditions
40 (Arsenault et al. 2018; Osman et al. 2022b; Chiang et al. 2018; Seneviratne et al. 2010; Miralles
41 et al. 2019). However, many operational forecasting systems, particularly subseasonal-to-
42 seasonal (S2S) models, lack a dynamic representation of vegetation, limiting their ability to
43 accurately simulate the intricate feedbacks that govern flash drought intensification (Pendergrass
44 et al. 2020). The accurate representation of vegetation dynamics is crucial across various
45 modeling time scales, from short-term numerical weather prediction (NWP) to longer-term
46 climate models for enhancing flash drought prediction and early warning capabilities.

47 Recent studies have highlighted the complex impact of vegetation on flash drought development
48 and evolution. For instance, research has shown that the presence of vegetation can influence soil
49 moisture depletion rates, with densely vegetated areas exhibiting higher susceptibility to flash
50 droughts due to increased evapotranspiration under hot and dry conditions, directly driving the
51 surface water balance towards low moisture conditions (Jiang et al. 2024; Zhang et al. 2021). At
52 the same time, it is also possible that dense vegetation can, in some cases, access deeper soil
53 moisture reserves, potentially mitigating the impact of near-surface drying. Additionally, the type
54 and health of vegetation can affect the surface energy balance, altering the partitioning between
55 sensible and latent heat fluxes and potentially amplifying atmospheric warming and drought
56 intensification (Osman et al. 2022b; Miralles et al. 2019). The dynamic nature of vegetation,
57 including changes in leaf area index (LAI) and the complex response of stomatal conductance to
58 water stress, can further modulate land-atmosphere feedbacks during flash droughts (Niu et al.

59 2011; Parazoo et al. 2024). These vegetation-driven feedbacks can influence atmospheric
60 circulation patterns, cloud formation, and precipitation, potentially leading to self-propagating
61 droughts where initial soil moisture deficits trigger a cascade of atmospheric and land surface
62 drying (Koster et al. 2019; Schumacher et al. 2022; Miralles et al. 2019; Entekhabi 2023).

63 The critical role of vegetation in flash droughts is further emphasized by studies demonstrating
64 the limitations of models that rely on climatological vegetation inputs. The use of climatological
65 vegetation, instead of dynamic vegetation, is a simplification that can hinder all models and
66 forecast lead times to a struggle to capture the interannual variability of evapotranspiration and
67 land water and energy states. In this study we are concerned with the impact this simplification
68 has for S2S prediction, but it also creates challenges for NWP and climate models attempting to
69 simulate rapidly emerging drought conditions and their feedback on vegetation growth and
70 health (Ukkola et al. 2016a,b; Tallaksen and Stahl 2014). Consequently, the integration of
71 remotely sensed vegetation observations, such as LAI, into land surface models has shown
72 promise in improving drought characterization. Mocko et al. (2021) demonstrated that
73 assimilating LAI data into the Noah-MP land surface model led to substantial improvements in
74 simulating agricultural drought. Similarly, Nie et al. (2022) and Fallah et al. (2024) highlighted
75 the benefits of LAI assimilation in capturing the spatial distribution of vegetation response to
76 drought and improving the simulation of transpiration and associated carbon fluxes and potential
77 transition to longer-term droughts. Furthermore, Ahmad et al. (2022) emphasized the necessity of
78 incorporating multiple observational constraints, including both soil moisture and vegetation
79 properties, to effectively capture the rapid onset and intensification of flash droughts driven by
80 different mechanisms. They also highlighted the importance of capturing the "flashiness" of
81 these droughts, characterized by rapid rates of soil moisture decline and vegetation stress.

82 The 2011 Texas flash drought, marked by its exceptional intensity and widespread impacts,
83 serves as a compelling case study for investigating the role of vegetation in flash drought
84 modeling (Nielsen-Gammon 2012). While the overall event resulted in the driest 12-month
85 period on record for the state, with an average of slightly more than 11 inches of rainfall
86 compared to the normal 27-inch average (Nielsen-Gammon 2012), it was the rapid onset and
87 intensification within this period that defines the flash drought. This intensification was primarily
88 driven by a persistent lack of precipitation coupled with record-breaking temperatures (Nielsen-

89 Gammon 2012). The severity of the drought was amplified by antecedent wet conditions in the
90 spring of 2011, which promoted lush vegetation growth that subsequently dried out, providing
91 ample fuel for devastating wildfires and exacerbating soil moisture depletion (Nielsen-Gammon
92 2012; Schwantes et al. 2016; Yang 2013; Adhikari et al. 2024). The agricultural sector
93 experienced catastrophic losses, exceeding \$7.62 billion, due to widespread crop failures,
94 reduced livestock productivity, and increased supplemental feeding costs (Nielsen-Gammon
95 2012). The ecological repercussions were also severe, with extensive tree mortality observed
96 across central and eastern Texas, impacting both managed and natural ecosystems (Lawal et al.
97 2024; Nielsen-Gammon 2012). The drought's intensity was unprecedented, with the Palmer
98 Drought Severity Index (PDSI), a comprehensive measure of drought intensity, reaching record-
99 low values, surpassing even the infamous drought of the 1950s in its severity (Nielsen-Gammon
100 2012). The extreme heat during the summer months further intensified drought conditions,
101 contributing to the rapid depletion of soil moisture and surface water resources, and highlighting
102 the complex interplay between meteorological, agricultural, and hydrological drought (Nielsen-
103 Gammon 2012; Wilhite et al. 2007).

104 While the 2011 Texas drought aligns with some characteristics of a 'heat wave flash drought' as
105 defined by Mo and Lettenmaier (2015), our model and satellite derived evapotranspiration
106 observations did not reveal the widespread increase in evapotranspiration (ET) typically
107 associated with the heatwave-driven flash drought events (Osman et al. 2022a). This suggests
108 that other factors, beyond simply high temperatures driving increased ET, played a more
109 dominant role in the rapid soil moisture depletion observed, which emphasizes the different
110 classes and pathways for the onset of flash droughts (Osman et al. 2022a) . The Southern Great
111 Plains, characterized by its strong land-surface-atmosphere coupling, is particularly susceptible
112 to such rapid drought intensification, as changes in vegetation and soil moisture can quickly
113 feedback into the atmosphere, influencing temperature, humidity, and ultimately precipitation
114 patterns (Basara and Christian 2018; Koster et al. 2004). This region's location in a transitional
115 zone between humid and arid climates, coupled with its extensive agricultural land cover and
116 reliance on rain-fed agriculture, further amplifies its vulnerability to flash droughts (Koster et al.
117 2004).

118 In this study, we delve into the influence of vegetation on the numerical modeling of flash
119 droughts, using the 2011 Texas event as a case study. We leverage the NU-WRF (Peters-Lidard
120 et al. 2007, 2015) and LIS modeling frameworks (Kumar et al. 2006) and the Noah-MP land
121 surface model (Niu et al. 2011; Yang et al. 2011) to examine the role of vegetation feedbacks on
122 the atmosphere in simulating the onset, severity, and land-atmosphere feedbacks associated with
123 this flash drought. We do this by integrating satellite-derived vegetation observations and
124 conducting controlled numerical experiments with modified vegetation parameters—that is,
125 rather than using a dynamic vegetation model, we prescribe vegetation condition based on
126 satellite-derived observations. This has the advantage of allowing us to look at model sensitivity
127 to observed vegetation stress rather than relying on the model’s own vegetation model to
128 simulate drought impacts on vegetation health. By doing this, we aim to rigorously evaluate the
129 model's ability to reproduce the observed characteristics of the 2011 Texas flash drought.
130 Through a deeper understanding of the role of vegetation as a mediator of flash drought, we can
131 pave the way for the development of more effective strategies to mitigate the impacts of these
132 devastating events on agriculture, water resources, and ecosystems in the Southern Great Plains
133 and beyond.

134

135 **Methods**

136 The NASA Unified-Weather Research and Forecasting (NU-WRF) model is a sophisticated
137 modeling system designed to simulate the complex interactions between the atmosphere, land
138 surface, aerosols, clouds, and precipitation at both satellite scales and the process level (Peters-
139 Lidard et al. 2015). It builds upon the widely-used Weather Research and Forecasting (WRF)
140 model (Skamarock et al. 2021), incorporating key NASA capabilities to enhance its
141 representation of Earth system processes.

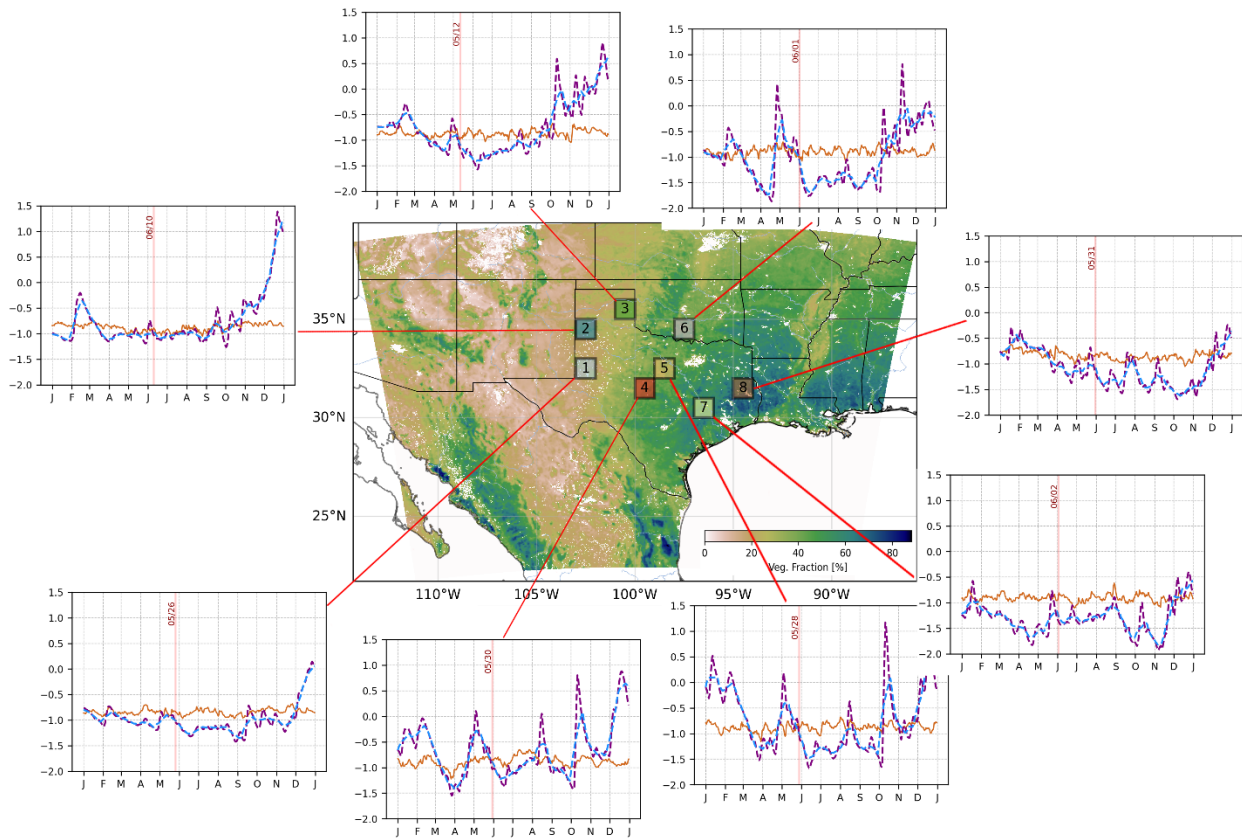
142 Crucially for our study on flash droughts, NU-WRF tightly couples the NASA Land Information
143 System (LIS) with the WRF atmospheric model, enabling a two-way exchange of information
144 between the land surface and the atmosphere (Peters-Lidard et al. 2015) that leverages the unique
145 assets of LIS. This coupling is therefore essential for capturing the dynamic feedbacks that drive
146 the rapid onset and intensification of flash droughts, particularly in regions like the Southern
147 Great Plains where land-atmosphere interactions play a critical role. Furthermore, NU-WRF
148 integrates the Noah-MP land surface model, allowing for the explicit representation of vegetation
149 dynamics and their influence on soil moisture and surface energy fluxes.

150 By combining these advanced capabilities, NU-WRF provides a powerful platform for
151 investigating the influence of vegetation on flash drought modeling. The model's ability to
152 integrate satellite-derived vegetation observations and conduct controlled experiments with
153 modified vegetation parameters allows us to rigorously evaluate its performance in simulating
154 the 2011 Texas flash drought and gain deeper insights into the role of vegetation in these extreme
155 events.

156 The study focuses on the Southern Great Plains (SGP) region, including the state of Texas, USA
157 as shown in Figure 1. This region is characterized by its diverse land cover, ranging from semi-
158 arid grasslands in the west to humid forests in the east. The SGP experiences a continental
159 climate with hot summers and mild winters, making it prone to extreme weather events such as
160 heat waves and droughts. The 2011 Texas flash drought, which severely impacted the region's
161 agriculture, water resources, and ecosystems, serves as the focal point of this study. The region's
162 strong land-surface-atmosphere coupling, where changes in vegetation and soil moisture can
163 influence the surface fluxes that drive boundary layer evolution and atmospheric conditions

164 (Dirmeyer 2011), makes it a particularly challenging but relevant environment for investigating
165 the role of vegetation in flash drought modeling (Basara and Christian 2018; Koster et al. 2004).

166



167

168 *Figure 1: Map of the study domain encompassing the state of Texas, with eight analysis boxes*
169 *highlighted and numbered. The colors of these boxes correspond to the colors used to represent*
170 *each box in subsequent figures. The background depicts the climatological annual mean green*
171 *vegetation fraction (GVF) derived from MODIS observations, illustrating the spatial distribution*
172 *of vegetation cover across the region. Line-plots next to boxes represent the average flash*
173 *drought onset date for grid points within each box, as defined using the SMVI flash drought*
174 *index (Osman et al., 2024). The average flash drought onset dates for grid cells within each box*
175 *are marked with the vertical lines. Brown timeseries represent the 20th percentile RZSM, purple*
176 *and blue dashed-lines represent the 5 and 20 days running RZSM averages respectively, Y-axis is*
177 *the standardized RZSM anomaly.*

178 To capture the spatial heterogeneity of land-atmosphere interactions within this domain, we
179 define eight 1° by 1° analysis boxes (Figure 1), each representing a distinct geographical area
180 with potentially varying vegetation cover, including shrublands, savannas, grasslands, croplands,
181 and sparsely vegetated areas, within the detected flash drought regions during the 2011 event. We
182 excluded other land cover types, such as forests, urban or water, as these selected types are more
183 directly relevant to agricultural drought, the primary focus of this study. These boxes,
184 strategically placed across the state of Texas, allow us to examine regional differences due to the
185 influence of vegetation status on flash drought intensification. The onset date for flash drought in
186 each box is drawn from our previously published inventory of flash droughts (Osman et al.,
187 2024). Briefly, Osman et al. (2024) defined flash drought onset based on a rapid decline in soil
188 moisture, exceeding a specified threshold within a short period. It is important to note that the
189 dates shown in Figure 1 represent the median flash drought onset date for grid points within each
190 box, reflecting the average timing of the event across the region, not a single, synchronous onset.

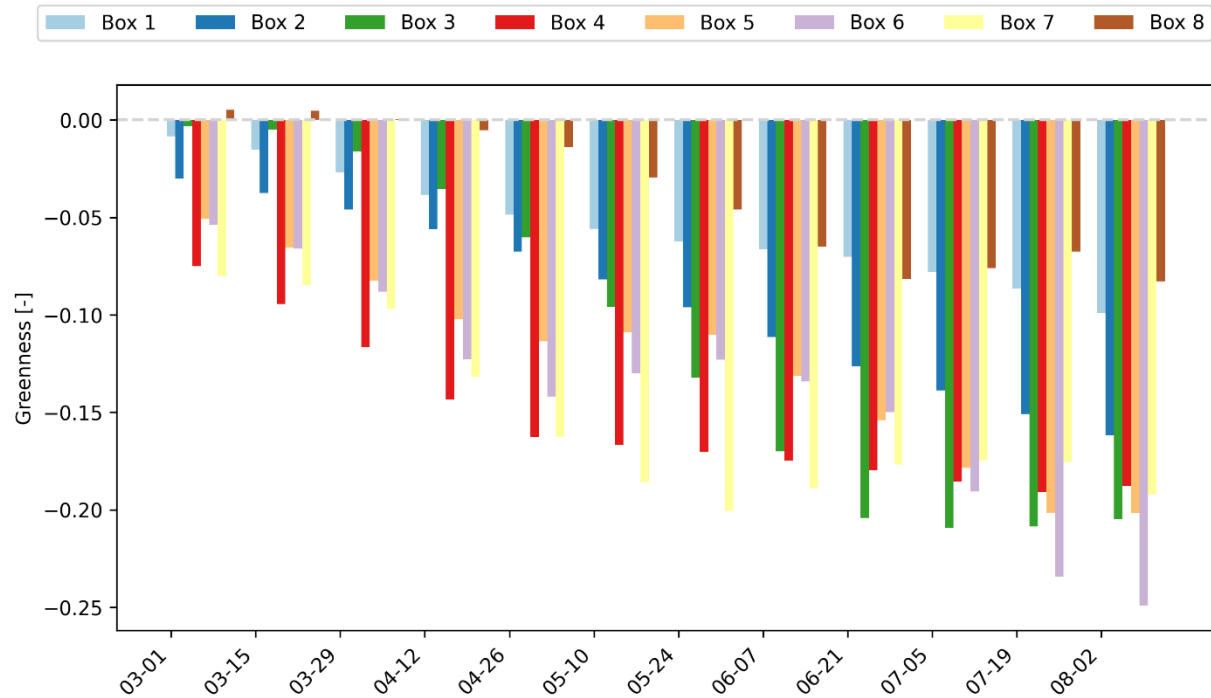
191 The model domain, covering a large portion of the Southern Great Plains and surrounding areas
192 at a 4-km horizontal resolution (covering approximately 2500km by 2000km), capturing
193 mesoscale features and regional variations in land surface and atmospheric conditions while
194 allowing for explicit representation of convection. The simulation period extends from March 1,
195 2011, to August 1, 2011, encompassing the antecedent conditions leading up to and the peak
196 intensification of the 2011 Texas flash drought event. Lateral boundary conditions are drawn
197 from Modern-Era Retrospective analysis for Research and Applications, Version 2 (MERRA-2)
198 reanalysis data. which provides a comprehensive reanalysis of the global atmosphere, land
199 surface, and ocean state, combining satellite observations with a numerical model to generate a
200 consistent and continuous record of meteorological variables (Gelaro et al. 2017).

201 To ensure an accurate representation of the land surface states at the beginning of the coupled
202 simulation, we conducted an initial 40-year spin-up run using LIS offline, driven by MERRA-2
203 reanalysis data. This spin-up process allows the land surface model to reach a state of
204 equilibrium, minimizing the influence of initial condition biases on the subsequent coupled
205 simulation.

206 For the atmospheric component, we implement NU-WRF using the Thompson microphysics
207 scheme (Thompson et al. 2008) and the Rapid Radiative Transfer Model for GCMs (RRTMG)

208 radiation scheme (Iacono et al. 2008). The Thompson scheme simulates the formation and
209 evolution of various hydrometeors (e.g., cloud water, rain, ice, snow) within the atmosphere,
210 while the RRTMG scheme calculates the transfer of solar and terrestrial radiation, both of which
211 are critical factors influencing the energy balance and water cycle during flash droughts. The
212 MYNN2.5 planetary boundary layer (PBL) scheme is used to parameterize the vertical turbulent
213 mixing of momentum, heat, and moisture in the atmosphere, solving a prognostic equation for
214 turbulent kinetic energy (TKE) to determine eddy diffusivities (Nakanishi and Niino 2006, 2009;
215 Olson et al. 2019). This combination of physics routines has performed well in previous studies
216 of Southern Great Plains atmospheric dynamics (Squitieri and Gallus 2016).

217 In this study, the Noah-MP land surface model (Niu et al. 2011; Yang et al. 2011) within LIS is
218 configured with four soil layers and employs climatological MODIS green vegetation fraction
219 (GVF) data in one experiment and GVF data that includes interannual variability (Nie et al.
220 2018) in another, enabling us to assess the impact of dynamic vegetation representation on flash
221 drought simulations. Both the climatological (CLIM) and interannually varying (IVAR) GVF
222 datasets are based on MODIS NDVI composites at a 0.05° spatial resolution from January 2002
223 to present (Nie et al. 2018) using the GVF estimation algorithm of Case et al. (2014). Figure 2
224 shows the bi-weekly averaged difference in GVF between IVAR and CLIM for eight analysis
225 boxes. As indicated in the figure, IVAR generally has lower GVF than CLIM during the study
226 period ranging up to a 25% drop in vegetation fraction.



227

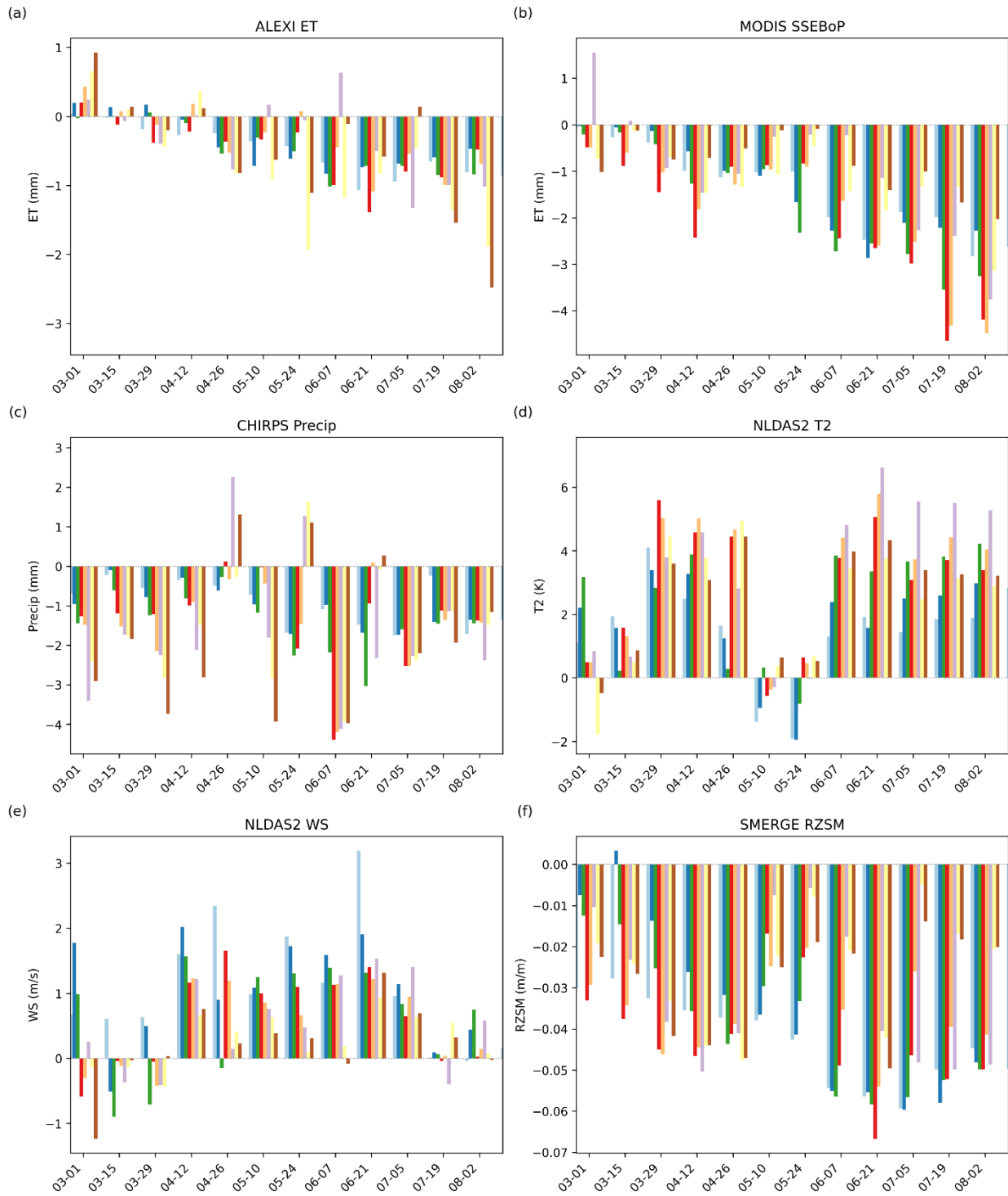
228 *Figure 2: Difference in bi-weekly averaged Green Vegetation Fraction (GVF) between the*
 229 *interannually-varying vegetation experiment (IVAR) and the climatological vegetation*
 230 *experiment (CLIM; the 2001-2017 average) for the eight analysis boxes. Colors correspond to*
 231 *the analysis box colors in Figure 1. A negative difference indicates that the IVAR experiment*
 232 *shows lower GVF, as prescribed from observations, compared to the CLIM experiment.*

233 In addition to the coupled NU-WRF simulations, we perform offline LIS simulations using the
 234 same implementation of Noah-MP. This allows us to compare representation of surface
 235 conditions during the drought in coupled and uncoupled simulations. For the offline simulations
 236 the primary meteorological forcing for the simulations is derived from the MERRA-2 reanalysis
 237 data. However, to improve the representation of precipitation, the Integrated Multi-satellitE
 238 Retrievals (IMERG) for NASA Global Precipitation Measurement (GPM) - GPM IMERG -
 239 precipitation data (Huffman et al. 2020) is used to replace the MERRA-2 precipitation forcing, as
 240 it offers high-resolution precipitation estimates that merge data from multiple satellite platforms
 241 and ground-based observations. In addition to providing a set of offline comparison simulations
 242 during the study period, this implementation of LIS provided surface initial conditions for the
 243 NU-WRF simulations. All offline simulations used in the simulation were spun up for 40 years
 244 prior to the start of the study period to allow model soil moisture to reach equilibrium.

245 **Results and Discussion**

246 *Observations of the 2011 drought*

247 The 2011 Texas flash drought manifested as a complex interplay of meteorological and land-
248 surface conditions, leading to rapid intensification and severe impacts across the Southern Great
249 Plains. As illustrated in Figure 3, NLDAS-2 2m temperature and 10m wind speed (Xia et al.
250 2012) (anomalies were calculated relative to a climatology period of 1979-2020), ALEXI
251 evapotranspiration (Anderson et al. 1997, 2007a,b) (anomalies were calculated relative to a
252 climatology period of 2001-2021), MODIS SSEBoP evapotranspiration (Senay et al. 2011, 2013)
253 (anomalies were calculated relative to a climatology period of 2000-2021), SMERGE root zone
254 soil moisture (Tobin et al. 2019) (anomalies were calculated relative to a climatology period of
255 1979-2016) and CHIRPS precipitation data (Funk et al. 2015) (anomalies were calculated
256 relative to a climatology period of 1981-2023) reveal key characteristics of this event and its
257 evolution within the study domain.



258

259

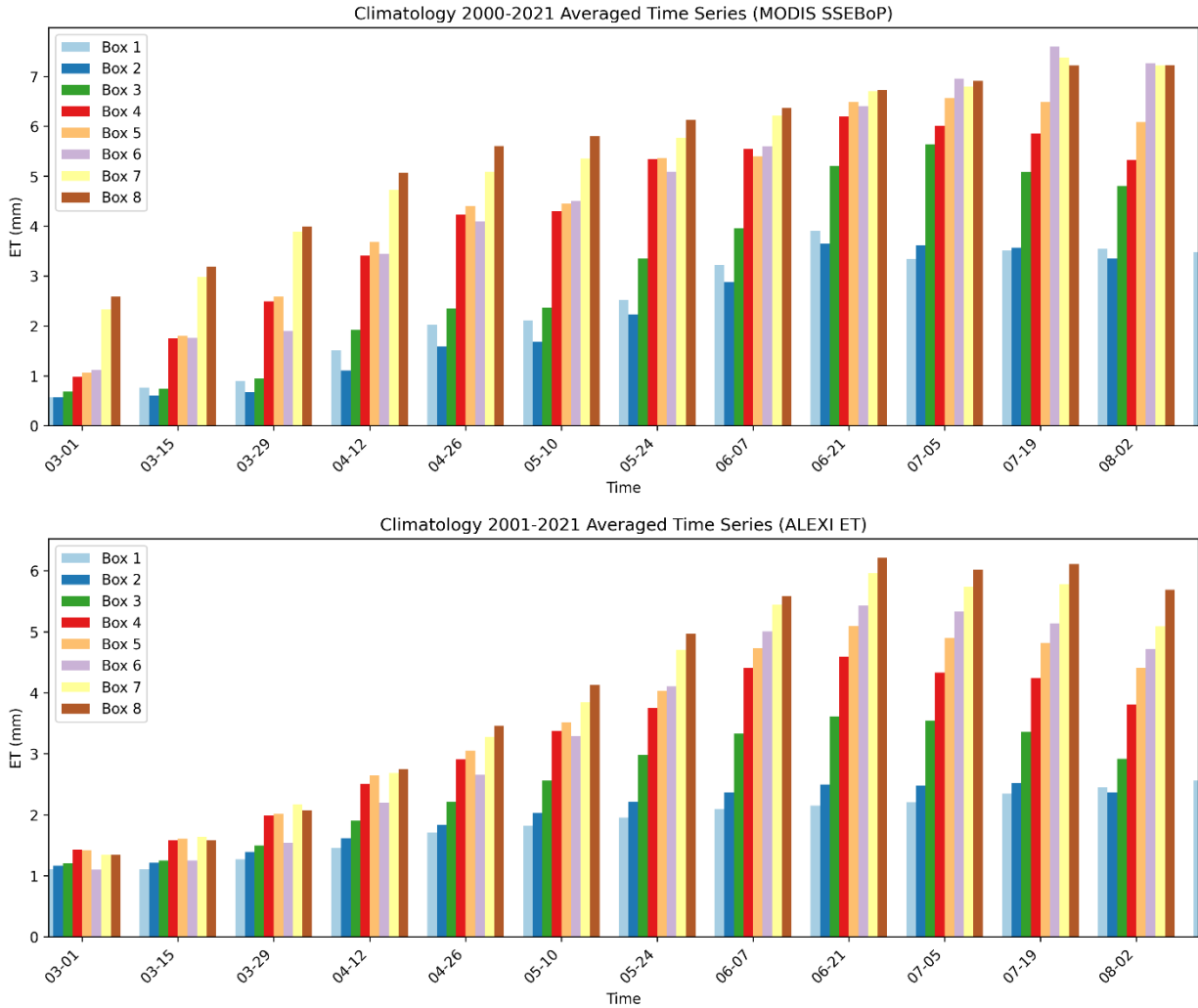
260 *Figure 3: Bar charts of the difference in bi-weekly averaged observed atmospheric and land*
261 *surface anomaly conditions during the study period from March 1st to August 1st compared to the*
262 *long-term climatology for the used datasets of each plot. Note that the climatology periods vary*
263 *depending on data availability.*

264 The plot of 2m temperature anomalies (Figure 3-d) highlights the dramatic warming trend during
265 the spring and summer of 2011. Positive anomalies began to emerge in April, with peak
266 anomalies exceeding 6°C in some boxes. Conditions in May were mixed, with an average of two
267 weeks relief from the observed abnormally hot conditions, though still warmer than average over
268 the month. From late May onward anomalous warmth persisted throughout the summer,
269 contributing to increased evaporative demand and exacerbating drought conditions. It is
270 important to note that while these temperature anomalies suggest that dry conditions were
271 present from early in the year, flash drought is specifically defined by the rapid decline in
272 RZSM. Anomalously high temperatures, winds, and precipitation deficits can be contributing
273 factors to flash drought (Otkin et al. 2018; Osman et al. 2022a; Chen et al. 2019), but the key
274 characteristic is the rapid root zone soil moisture loss. Furthermore, there can be multiple flash
275 drought episodes within a year if there are temporary recoveries in soil moisture (Osman et al.
276 2024). In this analysis, we are primarily focused on the most intense, widespread flash drought
277 event that occurred during the summer months.

278 The climatology of evapotranspiration (ET) exhibits a typical seasonal pattern, with values
279 increasing from spring to summer (Figure 4). However, the 2011 actual ET curves (Figures 3-a &
280 3-b) deviate significantly from this expected trend. Despite some slightly positive anomalies in
281 early spring, a sharp decline in ET emerges from May onwards, coinciding with the onset of the
282 flash drought. This decline reflects the vegetation's response to rapidly depleting soil moisture
283 and increasing atmospheric demand, ultimately reducing evapotranspiration rates. Notably, these
284 two diagnostic satellite products show no consistent evidence of enhanced springtime ET, a
285 characteristic sometimes associated with flash droughts. ALEXI has some indication of an ET
286 bump in early March, but it quickly fades, and MODIS SSEBoP doesn't show any at all. The
287 observed ET decline in late spring aligns with the period of rapid warming and precipitation
288 deficits, reinforcing the notion that land-atmosphere feedbacks, potentially modulated by

289 vegetation, may play a meaningful role during drought intensification (Seneviratne et al. 2010;
290 Miralles et al. 2019; Osman et al. 2022b).

291



292

293 *Figure 4: Bar charts of the climatological bi-weekly averaged observed evapotranspiration*
294 *derived from MODIS SSEBoP (Top) and ALEXI (Bottom) datasets during the study period from*
295 *March 1st to August 1st for the highlighted analysis boxes.*

296 In the context of our flash drought analysis, bi-weekly averaged precipitation anomalies for the
297 2011 flash drought, derived from the Climate Hazards Group InfraRed Precipitation with Station
298 data (CHIRPS) dataset for the period 1981-2021 (Figure 3-c), reveal a mixed pattern across the
299 study area. While some regions experienced persistent precipitation deficits throughout the

300 March-August period, others showed alternating periods of both deficit and surplus, highlighting
301 the heterogeneous nature of flash drought processes (Osman et al. 2021, 2022a).

302 The flash drought onset dates for each of the eight study regions, derived from the Soil Moisture
303 Volatility Index (SMVI) analysis presented in Osman et al. (2024) and illustrated in Figure 1,
304 spanned from mid-May to early June. While the SMVI analysis may identify multiple flash
305 drought episodes throughout the year, we primarily focus on the most intense, widespread events
306 that occurred during the summer months, as these have the most significant impact. . This timing
307 coincides with observed anomalies in key hydrometeorological variables, including temperature,
308 evapotranspiration, precipitation, and root-zone soil moisture (Figure 3). The rapid
309 intensification of drought conditions, characterized by sharp declines in soil moisture,
310 evapotranspiration, and mixed precipitation signals, underscores the "flashiness" of this event
311 and its potential for severe impacts. It is notable that the diagnosed rapidity of onset results, to
312 some extent, from the modest recovery period in early May: soil moisture deficits were flat or
313 somewhat reduced between late April and the third week of May, before increasing quickly and
314 dramatically during the period of diagnosed flash drought onset.

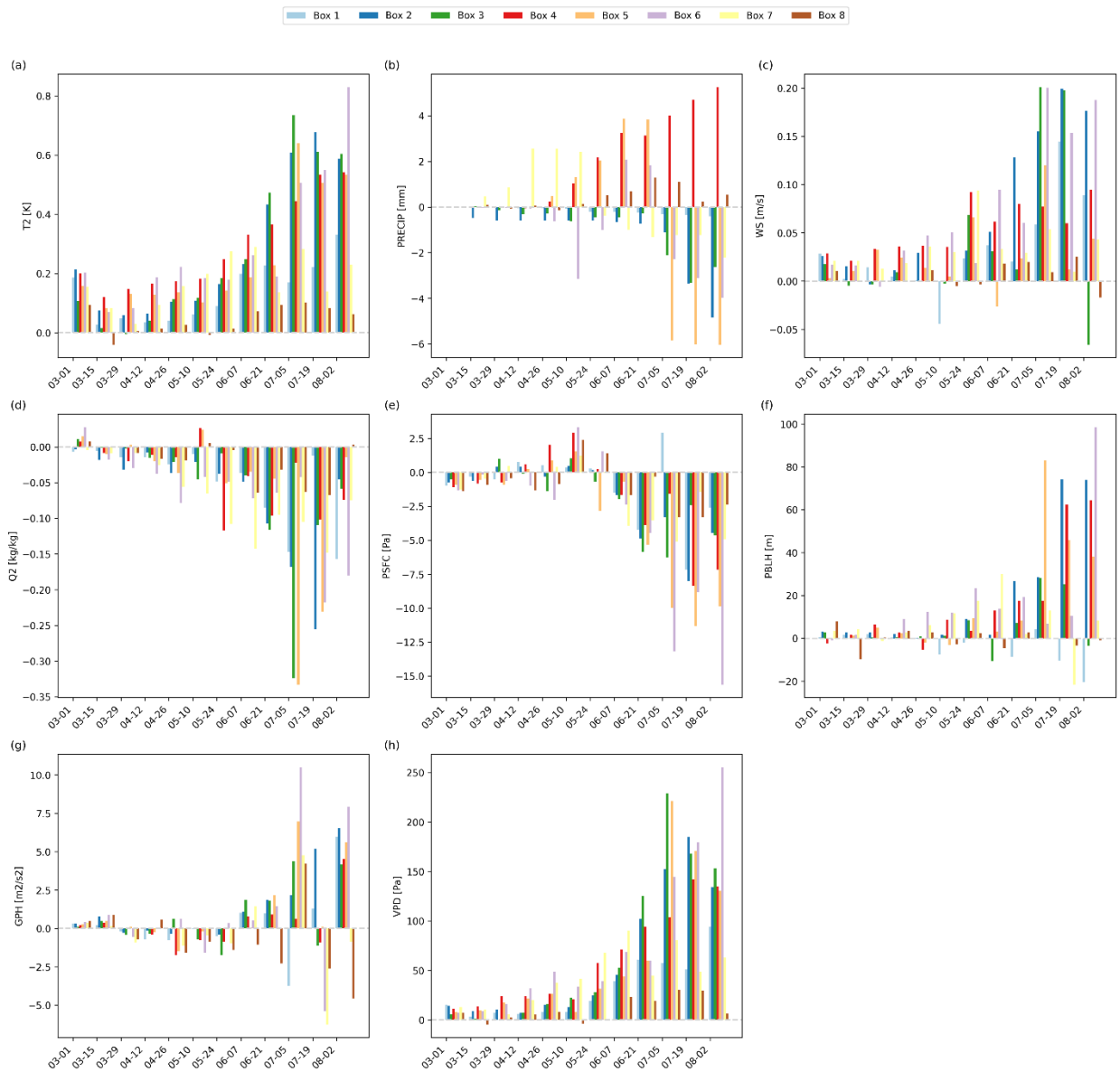
315 *NU-WRF Simulations*

316 We now turn to our simulation results, focusing on differences between the interannually-varying
317 vegetation simulation (IVAR) and the climatological vegetation simulation (CLIM) in coupled
318 NU-WRF runs. First, we examine what impact IVAR has on near-surface meteorology relative to
319 the CLIM simulation. Across most boxes and time periods, we observe positive 2-m air
320 temperature differences between simulations (IVAR - CLIM), indicating that the IVAR
321 experiment, which incorporates real-time vegetation information, generally simulates higher 2m
322 temperatures (T2) compared to the CLIM experiment (Figure 5a). This difference grows as the
323 drought reaches maturity, but it is present to some extent throughout the simulation period.
324 Impacts on precipitation are mixed (Figure 5b), as heterogeneity and mesoscale variability in
325 land-atmosphere interactions lead to localization of precipitation anomalies as opposed to region-
326 wide decreases in rainfall during the pre-drought and onset period.

327 Wind speeds tend to be higher (WS; Figure 5c), albeit by a modest amount in IVAR relative to
328 CLIM, reflecting greater mixing in the planetary boundary layer, while near-surface specific
329 humidity (Q2; Figure 5d) is substantially lower. This reduction in Q2, together with the increase

330 in T2, indicates lower relative humidity and increased vapor pressure deficit (VPD; Figure 5h).
331 IVAR also exhibits a deepened planetary boundary layer height (PBLH; Figure 5f) over time, as
332 a product of increased turbulence associated with higher surface temperatures and Bowen ratios
333 (sensible heat in favor of latent heat flux). There is some weaker expression of this in the mid-
334 troposphere, as 500 hPa geopotential height tends to be elevated in IVAR relative to CLIM
335 (GPH; Figure 5g).

336 It is tempting to compare plots of the difference between IVAR and CLIM simulations (like
337 Figure 5) to observed anomalies, as shown in Figure 3. But the two are not actually comparable.
338 Where observed anomalies show how 2011 differs from the average year, which could result
339 from any number of large-scale to local climate processes, comparisons of IVAR to CLIM show
340 only the simulated influence that anomalously low vegetation has on meteorological and
341 hydrological conditions. Figure 5a, for example, shows a consistent but modest warming
342 influence on temperature that increases as the drought merges and matures. According to
343 NLDAS (Figure 3d) temperature anomalies were substantially larger, and they did not show a
344 systematic increase during the drought. The two results are not necessarily inconsistent; the
345 counterfactual represented by the CLIM simulation (normal vegetation conditions under 2011
346 large-scale meteorology) is not directly observable.



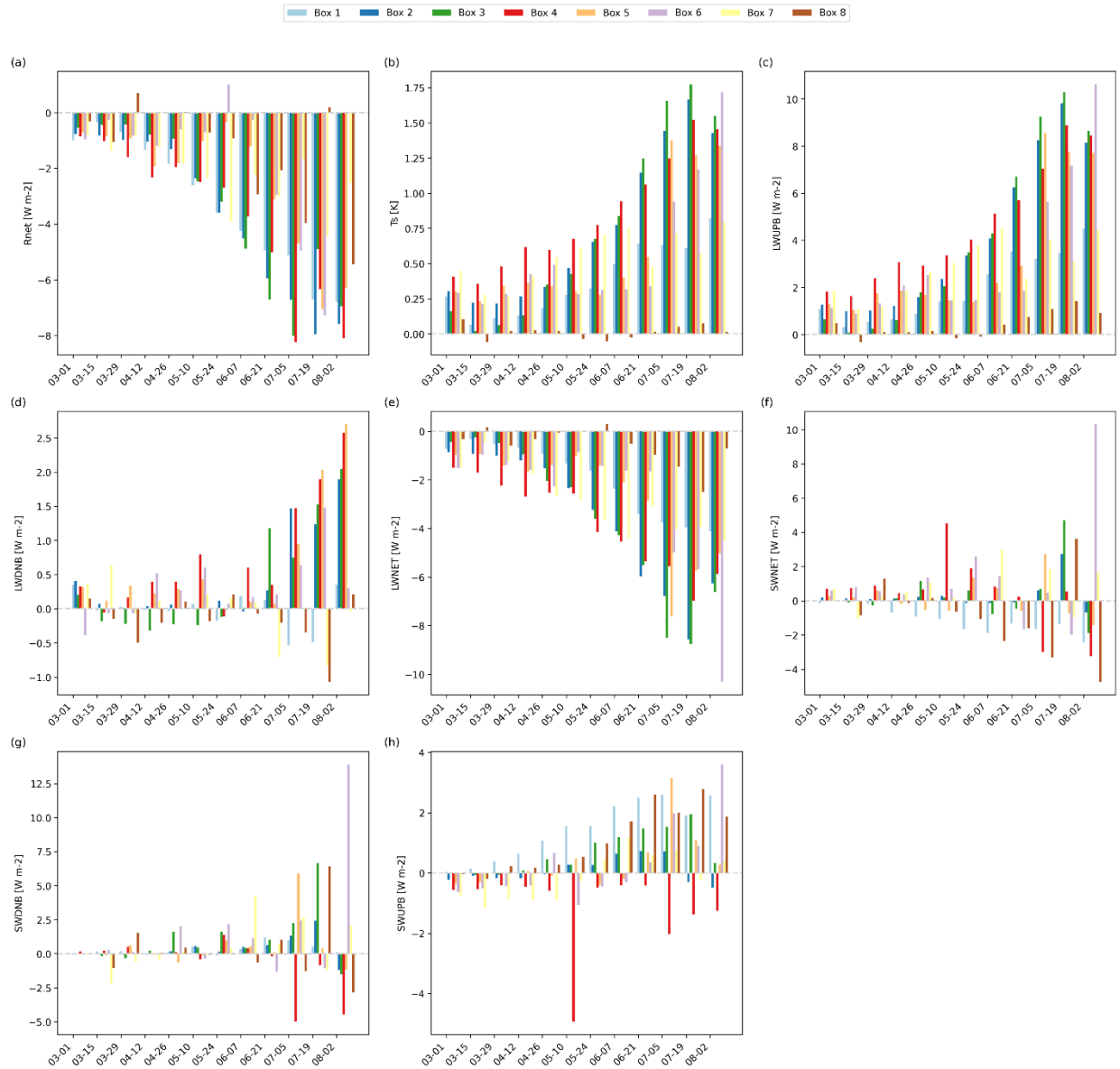
348

349 *Figure 5: Bar charts of the weekly averaged difference in near-surface meteorological fields*
 350 *between simulations using time-varying vegetation (IVAR) and climatological vegetation (CLIM)*
 351 *for the eight analysis boxes in the study area. (a) 2-meter air temperature (T2), (b) Precipitation*
 352 *(PRECIP), (c) 10-meter wind speed (WS), (d) Water vapor mixing ratio at 2m (Q2), (e) Surface*
 353 *pressure (PSFC), (f) Planetary boundary layer height (PBLH), (g) Geopotential height at 500*
 354 *hPa (GPH) and (h) Vapor pressure deficit (VPD).*

355 Turning to the surface energy budget, we see that accounting for vegetation impacts of the
 356 drought in IVAR leads to a decrease in net radiation at the surface relative to CLIM (Figure 6a).

357 This reduction is primarily attributable to higher surface temperatures (Figure 6b) that lead to
358 increased upwelling longwave radiation from the surface (Figure 6c) associated with the warmer
359 surface in IVAR simulations, and which is not fully compensated by increased downwelling
360 longwave radiation (Figure 6d), resulting in a decrease in net longwave radiation at the surface
361 (Figure 6e). The net shortwave radiation signal is mixed (Figure 6f) and is dominated by spatial
362 variability in downwelling shortwave radiation (Figure 6g). There is a tendency towards
363 increased reflected solar radiation (Figure 6h), but the reason for this is spatially variable: in
364 some areas it is simply a product of increased downwelling shortwave radiation, while in others
365 it is a result of drought-induced brightening of the surface (Zaitchik et al. 2013) – a phenomenon
366 that was patchy during this event and mostly emerged later in drought development.

367



368

369

370

371

372

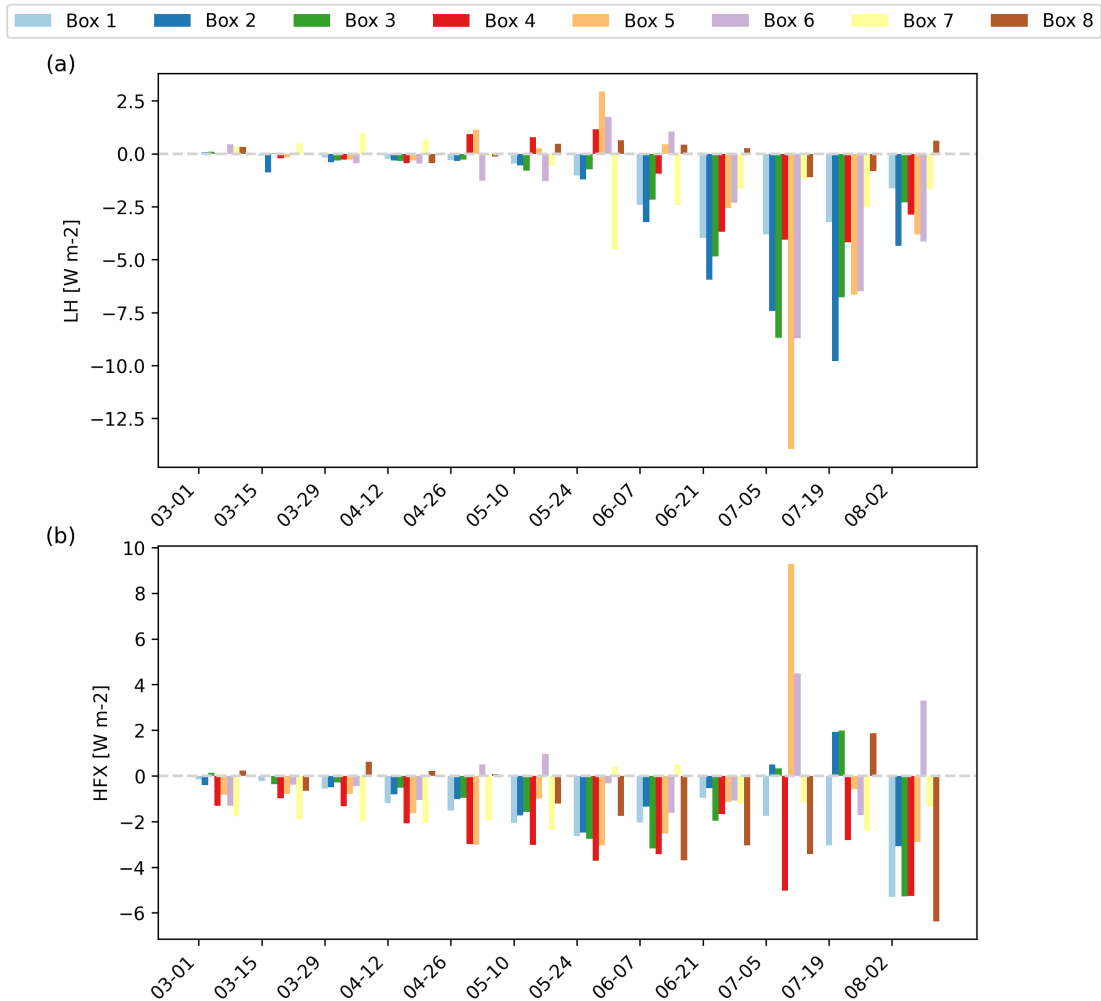
373

374

375

Figure 6: Bar charts of the Weekly averaged difference in radiation balance fields between simulations using interannually-varying vegetation (IVAR) and climatological vegetation (CLIM) for the eight analysis boxes in the study area. (a) Net radiation balance (R_{net}), (b) Surface temperature (T_s), (c) upward longwave radiation at the surface ($LWUPB$), (d) downward longwave radiation at the surface ($LWDNB$), (e) net longwave radiation ($LWNET$), (f) net shortwave radiation ($SWNET$), (g) downward shortwave radiation at the surface ($SWDNB$), and (h) upward shortwave radiation at the surface ($SWUPB$).

376 The drought also significantly alters turbulent energy fluxes, as evidenced by the pronounced
377 reduction in latent heat flux (i.e. evapotranspiration) (Figure 7a) and mixed signals (with an
378 overall slight reduction trend) in sensible heat flux (Figure 7b). This altered energy partitioning is
379 consistent with satellite-derived observations and with the simulated reduction in net radiation at
380 the surface (Figure 6a) and with a situation of water limitation: vapor pressure deficit and
381 potential evapotranspiration are increased, but accounting for vegetation die-back in IVAR
382 reduces simulated plant access to deeper soil moisture reserves, such that actual
383 evapotranspiration (or latent heat flux) is reduced. Both the latent and the sensible heat flux
384 difference develops primarily after drought initiation, indicating that the simulations do not show
385 a strong role of vegetation-mediated suppression of latent or sensible heat flux during the onset
386 of flash drought. The latent and sensible heat flux results are also consistent with previous
387 studies that have highlighted the potential for drought to lead to reduced net radiation and lower
388 energy conditions near the surface (Osman et al. 2022b; Miralles et al. 2019).



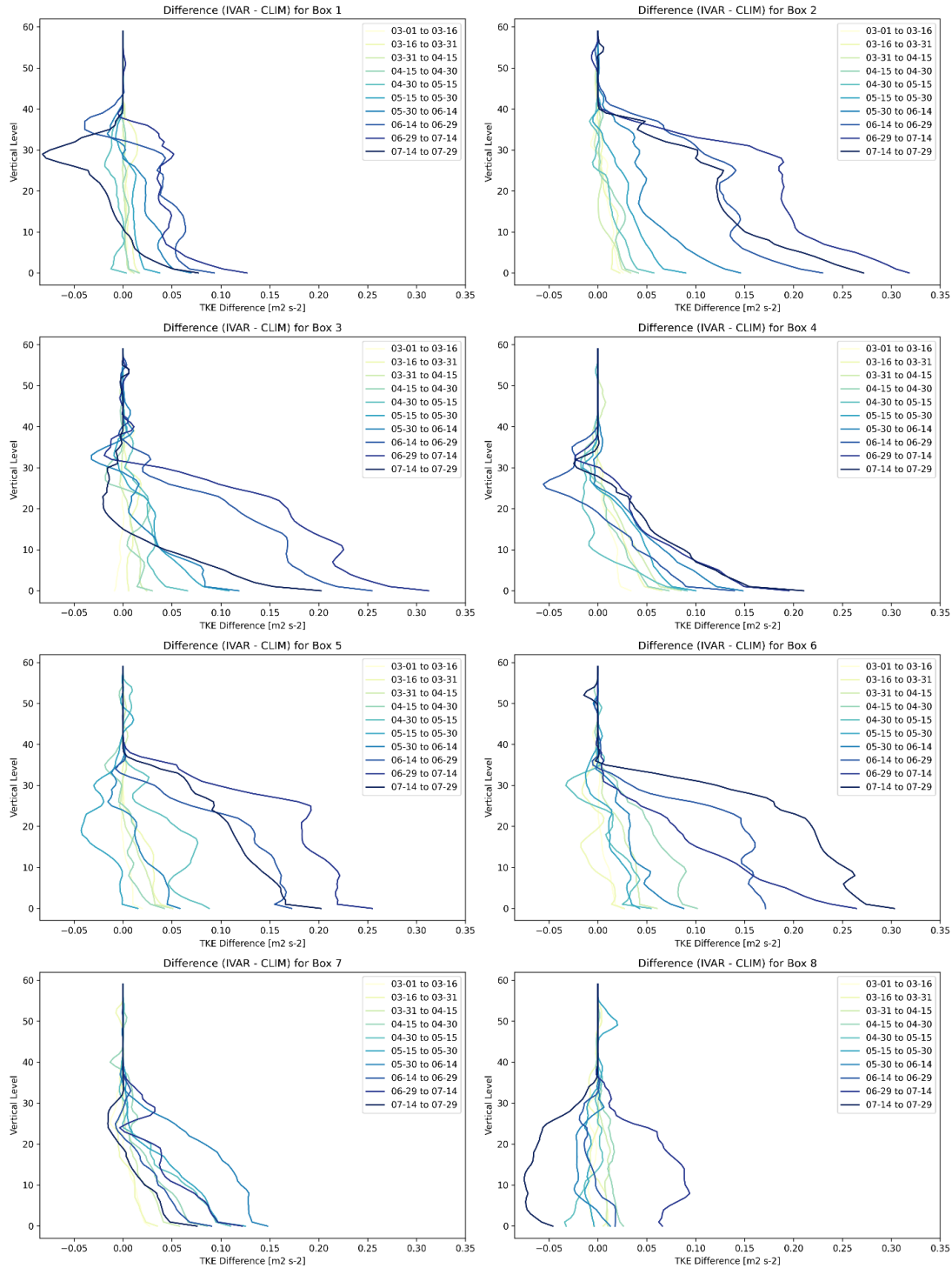
389

390 *Figure 7: Bar charts of the biweekly averaged difference in turbulent energy fluxes between*
 391 *simulations using interannually-varying vegetation (IVAR) and climatological vegetation (CLIM)*
 392 *for the eight analysis boxes in the study area. (a) Latent heat flux (LH), (b) Sensible heat flux*
 393 *(HFX).*

394 While the surface radiation and energy partitioning results are consistent with each other, it is
 395 interesting that the PBL is deeper in IVAR, particularly as the drought reaches maturity, even
 396 though surface turbulent energy fluxes are reduced. To explore this result, we examine
 397 atmospheric turbulence, as captured by turbulent kinetic energy (TKE) profiles. The vertical
 398 profiles of TKE differences between the IVAR and CLIM experiments (Figure 8) reveal how
 399 vegetation alters turbulence throughout the planetary boundary layer. Positive values indicate
 400 increased TKE in the IVAR experiment, suggesting that under drought stress, atmospheric
 401 turbulence is enhanced. The pattern extends as high as $\sim 5\text{km}$ above the surface (approximately

402 the 40th vertical model level). This is somewhat counterintuitive, given the reduction in surface
403 turbulent energy fluxes (sensible and latent heat flux) in IVAR relative to CLIM. However, both
404 longwave radiative heating of the boundary layer from the surface and regionally warmer
405 conditions in the IVAR simulation could contribute to higher PBL temperatures and greater TKE.
406 It's also important to consider that larger-scale atmospheric feedbacks, particularly during
407 heatwaves, may play a significant role. For example, the PBLH can more easily grow into a
408 warm, dry entrainment zone, especially over multiple days as conditions become drier and
409 warmer. In such situations, the PBL preconditions itself for rapid growth due to the residual
410 layer, potentially reducing the direct influence of surface forcing on TKE. Even if these
411 processes are not fully captured in turbulent energy fluxes between the surface and the lowest
412 model layer, they can still significantly influence TKE.

413 The spatial and temporal variability in TKE differences suggests that the influence of drought
414 conditions on atmospheric turbulence is most pronounced in transitional zones (Boxes 2-7) with
415 moderate vegetation cover, while it is less evident in both the most humid (Box 8) and most arid
416 (Box 1) regions. This is consistent with the spatial pattern of IVAR vs. CLIM differences in
417 several other fields (e.g., T2, Ts, LH) which also show largest impacts in the transitional zone
418 between humid areas with dense and deeply rooted vegetation (Box 8) and sparse vegetation in
419 arid regions (Box 1).



420

421 *Figure 8: Vertical profiles of differences in the turbulent kinetic energy (TKE) from the MYNN2.5*
 422 *planetary boundary layer scheme between the IVAR and CLIM experiments for the eight selected*
 423 *boxes in the Southern Great Plains averaged over 2-week time periods during the 2011 flash*
 424 *drought.*

425

426 **Conclusion**

427 The 2011 Texas flash drought, a landmark event in its intensity and widespread impacts,
428 occurred in a region hypothesized to have strong land-atmosphere coupling (Koster et al. 2004).
429 Here, we have investigated whether vegetation-mediated land-atmosphere feedbacks might have
430 played an important role in the drought's onset and development. In observation and controlled
431 numerical experiment, we find that the drought exhibits some but not all of the dynamics that
432 have been invoked in studies of flash drought process. The event does not, in remote sensing data
433 or simulation, show a strong pre-drought enhancement in ET. So, for this event, it does not
434 appear that early green-up and vegetation-driven soil moisture depletion played a major role in
435 priming the surface for drought. Once the drought began, however, we see that accounting for
436 drought impacts in vegetation—our IVAR simulation—results in reduced net radiation, lower
437 turbulent heat flux, higher vapor pressure deficit, and increased evaporative demand relative to a
438 simulation (CLIM) that does not account for these vegetation impacts. This suggests that, at least
439 within our modeling framework, vegetation feedbacks act to intensify meteorological conditions
440 that lead to vegetation stress.

441 These simulation results point to the potential value in of including drought-induced vegetation
442 dynamics in dynamically-based simulation and forecasting systems. In this study we prescribed
443 vegetation conditions based on observations, but in a forecast context one would need to include
444 a dynamic phenology model to capture these anomalies. In pointing to this potential, we
445 acknowledge that limited observations and the fact that we were not able to perform extended
446 multi-year NU-WRF simulations limit our ability to quantify the performance of IVAR relative
447 to CLIM. Rather, our conclusions are drawn from the fact that differences between IVAR and
448 CLIM are substantial and, in the case of observable variables, tend to be of the same sign as the
449 anomalies observed during the drought event.

450 Further research is required to explore the role of specific vegetation types and their
451 physiological responses to drought stress in modulating land-atmosphere feedbacks. From a
452 prediction standpoint, data assimilation (DA) offers a promising avenue for addressing the
453 challenges of incorporating these complex vegetation dynamics. The integration of additional
454 observational data, such as soil moisture and vegetation indices, through DA techniques, may

455 enhance model performance and capture the full spectrum of flash drought dynamics in real-time
456 forecasting. This approach could potentially reduce the reliance on dynamic vegetation models,
457 which are still a work in progress and face significant uncertainties in accurately representing
458 vegetation behavior. The insights gained from this study serve as a steppingstone towards a more
459 comprehensive and predictive understanding of flash droughts.

460 **References**

- 461 Adhikari, S., W. Zhou, Z. Dou, N. Sakib, R. Ma, B. Chaudhari, and B. Liu, 2024: Analysis of
462 Flash Drought and Its Impact on Forest Normalized Difference Vegetation Index (NDVI)
463 in Northeast China from 2000 to 2020. *Atmosphere*, **15**, 818,
464 <https://doi.org/10.3390/atmos15070818>.
- 465 Ahmad, S. K., and Coauthors, 2022: Flash Drought Onset and Development Mechanisms
466 Captured With Soil Moisture and Vegetation Data Assimilation. *Water Resour. Res.*, **58**,
467 1–17, <https://doi.org/10.1029/2022WR032894>.
- 468 Anderson, M. C., J. M. Norman, G. R. Diak, W. P. Kustas, and J. R. Mecikalski, 1997: A two-
469 source time-integrated model for estimating surface fluxes using thermal infrared remote
470 sensing. *Remote Sens. Environ.*, **60**, 195–216, [https://doi.org/10.1016/S0034-](https://doi.org/10.1016/S0034-4257(96)00215-5)
471 [4257\(96\)00215-5](https://doi.org/10.1016/S0034-4257(96)00215-5).
- 472 Anderson, M. C., J. M. Norman, J. R. Mecikalski, J. A. Otkin, and W. P. Kustas, 2007a: A
473 climatological study of evapotranspiration and moisture stress across the continental
474 United States based on thermal remote sensing: 1. Model formulation. *J. Geophys. Res.*
475 *Atmospheres*, **112**, 2006JD007506, <https://doi.org/10.1029/2006jd007506>.
- 476 ———, ———, ———, ———, and ———, 2007b: A climatological study of evapotranspiration and
477 moisture stress across the continental United States based on thermal remote sensing: 2.
478 Surface moisture climatology. *J. Geophys. Res. Atmospheres*, **112**, D11112,
479 <https://doi.org/10.1029/2006JD007507>.
- 480 Arsenault, K. R., G. S. Nearing, S. Wang, S. Yatheendradas, and C. D. Peters-Lidard, 2018:
481 Parameter sensitivity of the Noah-MP land surface model with dynamic vegetation. *J.*
482 *Hydrometeorol.*, **19**, 815–830, <https://doi.org/10.1175/JHM-D-17-0205.1>.
- 483 Basara, J. B., and J. I. Christian, 2018: Seasonal and interannual variability of land–atmosphere
484 coupling across the Southern Great Plains of North America using the North American
485 regional reanalysis. *Int. J. Climatol.*, **38**, 964–978, <https://doi.org/10.1002/joc.5223>.
- 486 Case, J. L., F. J. LaFontaine, J. R. Bell, G. J. Jedlovec, S. V. Kumar, and C. D. Peters-Lidard,
487 2014: A Real-Time MODIS Vegetation Product for Land Surface and Numerical Weather
488 Prediction Models. *IEEE Trans. Geosci. Remote Sens.*, **52**, 1772–1786,
489 <https://doi.org/10.1109/TGRS.2013.2255059>.
- 490 Chen, L. G., J. Gottschalck, A. Hartman, D. Miskus, R. Tinker, and A. Artusa, 2019: Flash
491 Drought Characteristics Based on U.S. Drought Monitor. *Atmosphere*, **10**, 498,
492 <https://doi.org/10.3390/atmos10090498>.
- 493 Chiang, F., O. Mazdinyasni, and A. AghaKouchak, 2018: Amplified warming of droughts in
494 southern United States in observations and model simulations. *Sci. Adv.*, **4**, eaat2380,
495 <https://doi.org/10.1126/sciadv.aat2380>.

- 496 Dirmeyer, P. A., 2011: The terrestrial segment of soil moisture-climate coupling: SOIL
497 MOISTURE-CLIMATE COUPLING. *Geophys. Res. Lett.*, **38**, n/a-n/a,
498 <https://doi.org/10.1029/2011GL048268>.
- 499 Entekhabi, D., 2023: Propagation in the Drought Cascade: Observational Analysis Over the
500 Continental US. *Water Resour. Res.*, **59**, e2022WR032608,
501 <https://doi.org/10.1029/2022WR032608>.
- 502 Fallah, A., M. A. Barlow, L. Agel, J. Kim, J. Mankin, D. M. Mocko, and C. B. Skinner, 2024:
503 Impact of Vegetation Assimilation on Flash Drought Characteristics across the
504 Continental United States. *J. Hydrometeorol.*, **25**, 1263–1281,
505 <https://doi.org/10.1175/JHM-D-23-0219.1>.
- 506 Funk, C., and Coauthors, 2015: The climate hazards infrared precipitation with stations—a new
507 environmental record for monitoring extremes. *Sci. Data*, **2**, 150066,
508 <https://doi.org/10.1038/sdata.2015.66>.
- 509 Gelaro, R., and Coauthors, 2017: The Modern-Era Retrospective Analysis for Research and
510 Applications, Version 2 (MERRA-2). *J. Clim.*, **30**, 5419–5454,
511 <https://doi.org/10.1175/JCLI-D-16-0758.1>.
- 512 Huffman, G. J., and Coauthors, 2020: Integrated Multi-satellite Retrievals for the Global
513 Precipitation Measurement (GPM) Mission (IMERG). *Satellite Precipitation
514 Measurement: Volume 1*, V. Levizzani, C. Kidd, D.B. Kirschbaum, C.D. Kummerow, K.
515 Nakamura, and F.J. Turk, Eds., Springer International Publishing, 343–353,
516 https://doi.org/10.1007/978-3-030-24568-9_19.
- 517 Iacono, M. J., J. S. Delamere, E. J. Mlawer, M. W. Shephard, S. A. Clough, and W. D. Collins,
518 2008: Radiative forcing by long-lived greenhouse gases: Calculations with the AER
519 radiative transfer models. *J. Geophys. Res. Atmospheres*, **113**, 2008JD009944,
520 <https://doi.org/10.1029/2008JD009944>.
- 521 Jiang, Y., H. Shi, Z. Wen, X. Yang, Y. Wu, and L. Li, 2024: Monitoring of Flash Drought on the
522 Loess Plateau and Its Impact on Vegetation Ecosystems,
523 <https://doi.org/10.3390/fl5081455>.
- 524 Koster, R. D., and Coauthors, 2004: Regions of strong coupling between soil moisture and
525 precipitation. *Science*, **305**, 1138–1140, <https://doi.org/10.1126/science.1100217>.
- 526 Koster, R. D., S. D. Schubert, H. Wang, S. P. Mahanama, and A. M. Deangelis, 2019: Flash
527 drought as captured by reanalysis data: Disentangling the contributions of precipitation
528 deficit and excess evapotranspiration. *J. Hydrometeorol.*, **20**, 1241–1258,
529 <https://doi.org/10.1175/JHM-D-18-0242.1>.
- 530 Kumar, S. V., and Coauthors, 2006: Land information system: An interoperable framework for
531 high resolution land surface modeling. *Environ. Model. Softw.*, **21**, 1402–1415,
532 <https://doi.org/10.1016/J.ENVSOFT.2005.07.004>.

- 533 Lawal, S., J. Costanza, F. H. Koch, and R. M. Scheller, 2024: Modeling the impacts of hot
534 drought on forests in Texas. *Front. For. Glob. Change*, **7**,
535 <https://doi.org/10.3389/ffgc.2024.1280254>.
- 536 Miralles, D. G., P. Gentile, S. I. Seneviratne, and A. J. Teuling, 2019: Land–atmospheric
537 feedbacks during droughts and heatwaves: state of the science and current challenges.
538 *Ann. N. Y. Acad. Sci.*, **1436**, 19–35, <https://doi.org/10.1111/nyas.13912>.
- 539 Mocko, D. M., S. V. Kumar, C. D. Peters-Lidard, and S. Wang, 2021: Assimilation of vegetation
540 conditions improves the representation of drought over agricultural areas. *J.*
541 *Hydrometeorol.*, **22**, 1085–1098, <https://doi.org/10.1175/JHM-D-20-0065.1>.
- 542 Nakanishi, M., and H. Niino, 2006: An Improved Mellor–Yamada Level-3 Model: Its Numerical
543 Stability and Application to a Regional Prediction of Advection Fog. *Bound.-Layer*
544 *Meteorol.*, **119**, 397–407, <https://doi.org/10.1007/s10546-005-9030-8>.
- 545 ———, and ———, 2009: Development of an Improved Turbulence Closure Model for the
546 Atmospheric Boundary Layer. *J. Meteorol. Soc. Jpn. Ser II*, **87**, 895–912,
547 <https://doi.org/10.2151/jmsj.87.895>.
- 548 Nie, W., B. F. Zaitchik, M. Rodell, S. V. Kumar, M. C. Anderson, and C. Hain, 2018:
549 Groundwater Withdrawals Under Drought: Reconciling GRACE and Land Surface
550 Models in the United States High Plains Aquifer. *Water Resour. Res.*, **54**, 5282–5299,
551 <https://doi.org/10.1029/2017WR022178>.
- 552 ———, and Coauthors, 2022: Towards effective drought monitoring in the Middle East and North
553 Africa (MENA) region: implications from assimilating leaf area index and soil moisture
554 into the Noah-MP land surface model for Morocco. *Hydrol. Earth Syst. Sci.*, **26**, 2365–
555 2386, <https://doi.org/10.5194/hess-26-2365-2022>.
- 556 Nielsen-Gammon, J., 2012: The 2011 Texas Drought. *Tex. Water J.*, **3**, 59–95,
557 <https://doi.org/10.21423/twj.v3i1.6463>.
- 558 Niu, G.-Y., and Coauthors, 2011: The community Noah land surface model with
559 multiparameterization options (Noah-MP): 1. Model description and evaluation with
560 local-scale measurements. *J. Geophys. Res.*, **116**, D12109,
561 <https://doi.org/10.1029/2010JD015139>.
- 562 Olson, J. B., J. S. Kenyon, Wayne. A. Angevine, J. M. Brown, M. Pagowski, and K. Sušelj, 2019:
563 A Description of the MYNN-EDMF Scheme and the Coupling to Other Components in
564 WRF–ARW, <https://doi.org/10.25923/N9WM-BE49>.
- 565 Osman, M., B. F. Zaitchik, H. S. Badr, J. I. Christian, T. Tadesse, J. A. Otkin, and M. C.
566 Anderson, 2021: Flash drought onset over the contiguous United States: sensitivity of
567 inventories and trends to quantitative definitions. *Hydrol. Earth Syst. Sci.*, **25**, 565–581,
568 <https://doi.org/10.5194/hess-25-565-2021>.

- 569 ———, and Coauthors, 2022a: Diagnostic Classification of Flash Drought Events Reveals Distinct
570 Classes of Forcings and Impacts. *J. Hydrometeorol.*, **23**, 275–289,
571 <https://doi.org/10.1175/JHM-D-21-0134.1>.
- 572 Osman, M., B. F. Zaitchik, and N. S. Winstead, 2022b: Cascading Drought-Heat Dynamics
573 During the 2021 Southwest United States Heatwave. *Geophys. Res. Lett.*, **49**,
574 e2022GL099265, <https://doi.org/10.1029/2022GL099265>.
- 575 Osman, M., B. Zaitchik, J. Otkin, and M. Anderson, 2024: A global flash drought inventory
576 based on soil moisture volatility. *Sci. Data*, **11**, 965, [https://doi.org/10.1038/s41597-024-](https://doi.org/10.1038/s41597-024-03809-9)
577 [03809-9](https://doi.org/10.1038/s41597-024-03809-9).
- 578 Otkin, J. A., M. C. Anderson, C. Hain, I. E. Mladenova, J. B. Basara, and M. Svoboda, 2013:
579 Examining Rapid Onset Drought Development Using the Thermal Infrared–Based
580 Evaporative Stress Index. *J. Hydrometeorol.*, **14**, 1057–1074,
581 <https://doi.org/10.1175/JHM-D-12-0144.1>.
- 582 ———, M. Svoboda, E. D. Hunt, T. W. Ford, M. C. Anderson, C. Hain, and J. B. Basara, 2018:
583 Flash Droughts: A Review and Assessment of the Challenges Imposed by Rapid-Onset
584 Droughts in the United States. *Bull. Am. Meteorol. Soc.*, **99**, 911–919,
585 <https://doi.org/10.1175/BAMS-D-17-0149.1>.
- 586 Parazoo, N., M. Osman, M. Pascolini-Campbell, and B. Byrne, 2024: Antecedent Conditions
587 Mitigate Carbon Loss During Flash Drought Events. *Geophys. Res. Lett.*, **51**,
588 <https://doi.org/10.1029/2024GL108310>.
- 589 Pendergrass, A. G., and Coauthors, 2020: Flash droughts present a new challenge for
590 subseasonal-to-seasonal prediction. *Nat. Clim. Change*, **10**, 191–199,
591 <https://doi.org/10.1038/s41558-020-0709-0>.
- 592 Peters-Lidard, C. D., and Coauthors, 2007: High-performance Earth system modeling with
593 NASA/GSFC’s Land Information System. *Innov. Syst. Softw. Eng.*, **3**, 157–165,
594 <https://doi.org/10.1007/s11334-007-0028-x>.
- 595 ———, and Coauthors, 2015: Integrated modeling of aerosol, cloud, precipitation and land
596 processes at satellite-resolved scales. *Environ. Model. Softw.*, **67**, 149–159,
597 <https://doi.org/10.1016/j.envsoft.2015.01.007>.
- 598 Schumacher, D. L., J. Keune, P. Dirmeyer, and D. G. Miralles, 2022: Drought self-propagation in
599 drylands due to land–atmosphere feedbacks. *Nat. Geosci.* **2022**, 1–7,
600 <https://doi.org/10.1038/s41561-022-00912-7>.
- 601 Schwantes, A. M., J. J. Swenson, and R. B. Jackson, 2016: Quantifying drought-induced tree
602 mortality in the open canopy woodlands of central Texas. *Remote Sens. Environ.*, **181**,
603 54–64, <https://doi.org/10.1016/j.rse.2016.03.027>.

- 604 Senay, G. B., M. E. Budde, and J. P. Verdin, 2011: Enhancing the Simplified Surface Energy
605 Balance (SSEB) approach for estimating landscape ET: Validation with the METRIC
606 model. *Agric. Water Manag.*, **98**, 606–618, <https://doi.org/10.1016/j.agwat.2010.10.014>.
- 607 Senay, G. B., S. Bohms, R. K. Singh, P. H. Gowda, N. M. Velpuri, H. Alemu, and J. P. Verdin,
608 2013: Operational Evapotranspiration Mapping Using Remote Sensing and Weather
609 Datasets: A New Parameterization for the SSEB Approach. *JAWRA J. Am. Water Resour.*
610 *Assoc.*, **49**, 577–591, <https://doi.org/10.1111/JAWR.12057>.
- 611 Seneviratne, S. I., T. Corti, E. L. Davin, M. Hirschi, E. B. Jaeger, I. Lehner, B. Orlowsky, and A.
612 J. Teuling, 2010: Investigating soil moisture–climate interactions in a changing climate: A
613 review. *Earth-Sci. Rev.*, **99**, 125–161, <https://doi.org/10.1016/j.earscirev.2010.02.004>.
- 614 Skamarock, W. C., and Coauthors, 2021: A Description of the Advanced Research WRF Model
615 Version 4.3. *NCAR Tech. Note*, **TN-556+STR**, 1–165, <https://doi.org/10.5065/1dfh-6p97>.
- 616 Squitieri, B. J., and W. A. Gallus, 2016: WRF Forecasts of Great Plains Nocturnal Low-Level
617 Jet-Driven MCSs. Part I: Correlation between Low-Level Jet Forecast Accuracy and
618 MCS Precipitation Forecast Skill. *Weather Forecast.*, **31**, 1301–1323,
619 <https://doi.org/10.1175/WAF-D-15-0151.1>.
- 620 Svoboda, M., and Coauthors, 2002: The Drought Monitor. *Bull. Am. Meteorol. Soc.*, **83**, 1181–
621 1190, <https://doi.org/10.1175/1520-0477-83.8.1181>.
- 622 Tallaksen, L. M., and K. Stahl, 2014: Spatial and temporal patterns of large-scale droughts in
623 Europe: Model dispersion and performance. *Geophys. Res. Lett.*, **41**, 429–434,
624 <https://doi.org/10.1002/2013GL058573>.
- 625 Thompson, G., P. R. Field, R. M. Rasmussen, and W. D. Hall, 2008: Explicit Forecasts of Winter
626 Precipitation Using an Improved Bulk Microphysics Scheme. Part II: Implementation of
627 a New Snow Parameterization. *Mon. Weather Rev.*, **136**, 5095–5115,
628 <https://doi.org/10.1175/2008MWR2387.1>.
- 629 Tobin, K. J., W. T. Crow, J. Dong, and M. E. Bennett, 2019: Validation of a New Root-Zone Soil
630 Moisture Product: Soil MERGE. *IEEE J. Sel. Top. Appl. Earth Obs. Remote Sens.*, **12**,
631 3351–3365, <https://doi.org/10.1109/JSTARS.2019.2930946>.
- 632 Ukkola, A. M., M. G. De Kauwe, A. J. Pitman, M. J. Best, G. Abramowitz, V. Haverd, M.
633 Decker, and N. Haughton, 2016a: Land surface models systematically overestimate the
634 intensity, duration and magnitude of seasonal-scale evaporative droughts. *Environ. Res.*
635 *Lett.*, **11**, <https://doi.org/10.1088/1748-9326/11/10/104012>.
- 636 Ukkola, A. M., A. J. Pitman, M. Decker, M. G. De Kauwe, G. Abramowitz, J. Kala, and Y. P.
637 Wang, 2016b: Modelling evapotranspiration during precipitation deficits: Identifying
638 critical processes in a land surface model. *Hydrol. Earth Syst. Sci.*, **20**, 2403–2419,
639 <https://doi.org/10.5194/hess-20-2403-2016>.

640 Wilhite, D. A., M. D. Svoboda, and M. J. Hayes, 2007: Understanding the Complex Impacts of
641 Drought: A Key to Enhancing Drought Mitigation and Preparedness,
642 <https://doi.org/10.1007/s11269-006-9076-5>.

643 Xia, Y., and Coauthors, 2012: Continental-scale water and energy flux analysis and validation for
644 the North American Land Data Assimilation System project phase 2 (NLDAS-2): 1.
645 Intercomparison and application of model products. *J. Geophys. Res. Atmospheres*, **117**,
646 n/a-n/a, <https://doi.org/10.1029/2011JD016048>.

647 Yang, Z., 2013: Developing a flash drought indicator for the US Great Plains. University of
648 Texas at Austin, 31pp., <http://hdl.handle.net/2152/21828>.

649 Yang, Z.-L., and Coauthors, 2011: The community Noah land surface model with
650 multiparameterization options (Noah-MP): 2. Evaluation over global river basins. *J.*
651 *Geophys. Res.*, **116**, D12110, <https://doi.org/10.1029/2010JD015140>.

652 Yuan, X., L. Wang, and E. F. Wood, 2018: Anthropogenic intensification of southern African
653 flash droughts as exemplified by the 2015/16 season. *Bull. Am. Meteorol. Soc.*, **99**, S86–
654 S90, <https://doi.org/10.1175/BAMS-D-17-0077.1>.

655 Zaitchik, B. F., J. A. Santanello, S. V. Kumar, and C. D. Peters-Lidard, 2013: Representation of
656 soil moisture feedbacks during drought in NASA unified WRF (NU-WRF). *J.*
657 *Hydrometeorol.*, **14**, 360–367, <https://doi.org/10.1175/JHM-D-12-069.1>.

658 Zhang, Y., Q. You, C. Chen, and X. Li, 2017: Flash droughts in a typical humid and subtropical
659 basin: A case study in the Gan River Basin, China. *J. Hydrol.*, **551**,
660 <https://doi.org/10.1016/j.jhydrol.2017.05.044>.

661 Zhang, Y., T. F. Keenan, and S. Zhou, 2021: Exacerbated drought impacts on global ecosystems
662 due to structural overshoot. *Nat. Ecol. Evol.* *2021 511*, **5**, 1490–1498,
663 <https://doi.org/10.1038/s41559-021-01551-8>.

664